JOURNAL OF SPACECRAFT AND ROCKETS
Vol. 39, No. 2, March–April 2002

Experimental and Numerical Investigation of Martian Atmosphere Entry

Diego Paterna,* Rodolfo Monti,† Raffaele Savino,‡ and Antonio Esposito§
University of Naples "Federico II," Naples 80125, Italy

A numerical and experimental investigation was performed to study the aerothermodynamic problems of entry into the Martian atmosphere. The mathematical and physical model used to study the flowfield around a capsule entering a CO_2 environment is described. Computational fluid dynamics tools have been applied to solve the system of governing equations. The importance of surface catalycity effects on the stagnation-point heat transfer and on the heat load in Martian atmosphere is highlighted. Stagnation-point heat flux levels applied to models of different materials in a plasma wind tunnel are shown, and numerical correlations are presented. The different role played by surface catalycity in Earth and Mars environments is shown.

Nomenclature

$\boldsymbol{A}_i$	=	ith face of the generic computational cell
A_k, β_k, E_k	=	constants appearing in the Arrhenius expression of the rate constant
B	=	ballistic coefficient, kg/m^2
C_i	=	molar concentration of species i
D	=	aerodynamic drag, N
D_i	=	diffusion coefficient of species i in the mixture
$D_{i,j}$	=	diffusion coefficient of species i in species j, m^2/s
E	=	specific total energy, J/kg
e	=	specific energy of the mixture
$e_{e,i}$	=	specific electronic energy of ith species, J/kg
e_i	=	specific internal energy of ith species, J/kg
$e_{\text{rot},i}$	=	specific rotational energy of ith species, J/kg
$e_{\text{tr},i}$	=	specific translational energy of ith species, J/kg
$e_{v,i}$	=	specific vibrational energy of species i, J/kg
$\boldsymbol{e}_{v,i}$	=	specific vibrational energy of ith species, J/kg
$\dot{e}_{v,i}$	=	vibrational source term, W/m^3
$e_{0,i}$	=	formation energy of ith species, J/kg
$\bar{\boldsymbol{F}}$	=	vector of the inviscid fluxes
$\bar{\boldsymbol{G}}$	=	vector of the viscous fluxes
$g_{1,i}$, $g_{2,i}$	=	degenerated modes
$\bar{\boldsymbol{H}}$	=	vector of the source terms
h_i	=	specific enthalpy of ith species, J/kg
$\boldsymbol{J}_i$	=	diffusive flux of ith species in the mixture, kg/(m^{2}s)
K_k	=	rate constant for reaction k (units depending on the reaction)
M^a, M^b	=	third-body efficiencies
M_i	=	molecular weight of ith species, kg/kg mol
m	=	vehicle mass, kg
m_i	=	mass fraction of ith species
p	=	pressure, Pa
p_i	=	partial pressure, Pa
Q	=	thermal load per unit area, J/cm^2
$Q_{e,i}$	=	electronic partition function
q, q_{NC}, q_{FC}	=	heat flux, noncatalytic, fully catalytic, W/cm^2
R_i	=	gas constant of ith species, J/(kgK)
R_0	=	universal gas constant [8314 J/(kgK)]
T	=	temperature, K
T_v	=	vibrational temperature, K
$T^c_{v,i}$	=	characteristic vibrational temperature of ith species, K
$\tilde{\boldsymbol{U}}$	=	vector of the fluid dynamic unkowns
$\underline{\boldsymbol{U}}$	=	unit tensor
V	=	vehicle velocity, m/s
V_c	=	cell volume
W	=	vehicle weight, N
Γ	=	total efficiency of third bodies
γ	=	flight-path angle with respect to the local horizon, deg
$\Theta_i(1)$, $\Theta_i(2)$	=	electronic characteristic temperatures, K
λ	=	thermal conductivity of the mixture, W/(mK)
λ_i	=	thermal conductivity of ith species, W/(mK)
μ	=	viscosity of the mixture, kg/(ms)
μ_i	=	viscosity of ith species, kg/(ms)
$\mu_{i,j}$	=	reduced molecular weight between species i and j, kg/kg mol
ν	=	stoichiometric coefficients
ρ	=	density, kg/m^3
σ	=	molecular cross section, cm^2
$\dot{\tau}_i$	=	vibrational relaxation time of species i in the mixture, s
$\dot{\tau}_{i,j}$	=	characteristic vibrational relaxation time of species i in species j, s
χ_r	=	molar fraction of species r
Ω	=	collisional integrals
$\dot{\omega}_i$	=	total reaction rate of species i, kg/(m^{3}s)
$\dot{\omega}_{i,k}$	=	reaction rate of species i in reaction k, kg/(m^{3}s)

Received 2 January 2001; presented as Paper 2001-0751 at the 38th Aerospace Sciences Meeting, Reno, NV, 8–11 January 2001; revision received 6 July 2001; accepted for publication 7 July 2001.

*Research Scientist, Department of Space Science and Engineering, "Luigi G. Napolitano."

†Full Professor of Aerodynamics, Department of Space Science and Engineering, "Luigi G. Napolitano." Member AIAA.

‡Associate Professor of Fluid Dynamics, Department of Space Science and Engineering, "Luigi G. Napolitano."

§Aerospace Engineer, Department of Space Science and Engineering, "Luigi G. Napolitano."

Introduction

INTERPLANETARY space programs show a clear interest in Mars exploration because the red planet is much more Earthlike than any other planet in our solar system. Apart from the Earth–moon system, Mars is the most hospitable body in the solar system and is currently the best candidate for future human exploration and colonization. Recent studies of crewed exploration missions to Mars have considered different scenarios. Each of these missions involves entry and aerocapture maneuvers both at Mars and at Earth on the return. Entry velocities at Mars and at Earth can vary greatly depending on the mission duration and whether the vehicle is crewed or uncrewed. Shown in Fig. 1 are Mars and Earth

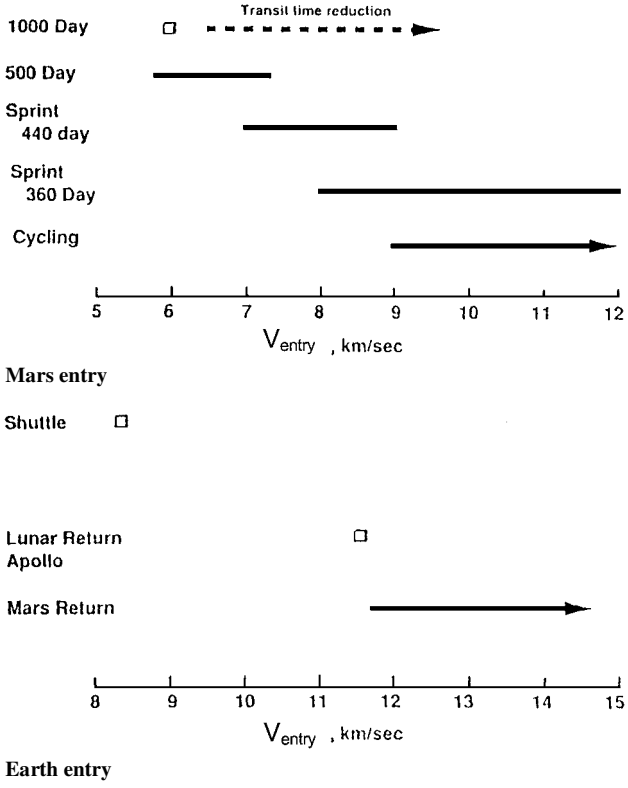

Fig. 1 Entry velocity envelopes for Mars missions with return to Earth.[1]

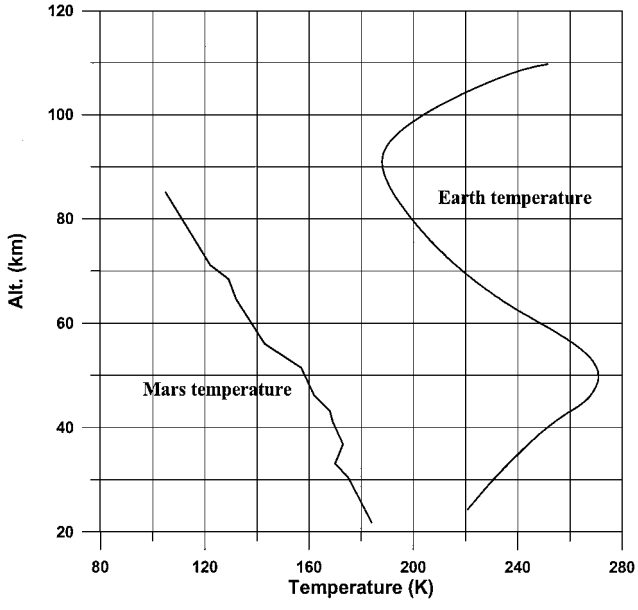

Fig. 2 Temperatures in Mars and Earth atmospheres.

entry velocity envelopes for various missions.[1] The purpose of outlining these mission scenarios is to illustrate the vast differences in flow physics, and hence aerothermal environment, that must be considered in the design of a hypersonic vehicle that must enter both Mars and Earth atmospheres. Indeed, major differences exist between the atmospheres of these two planets.

The atmosphere of Mars, which consists primarily of carbon dioxide at a relatively low pressure, is fairly well defined, although there are seasonal variations. In Figs. 2 and 3, the pressure and the temperature of the Mars atmosphere are compared with those of the Earth.

Heat fluxes and thermal loads, that is, the time integrals of heat flux, encountered by a module entering the atmosphere are key issues in determining the type and size of the thermal protection system. Real-gas thermochemical nonequilibrium processes are fundamental in the determination of aerodynamic heating. A blunt-

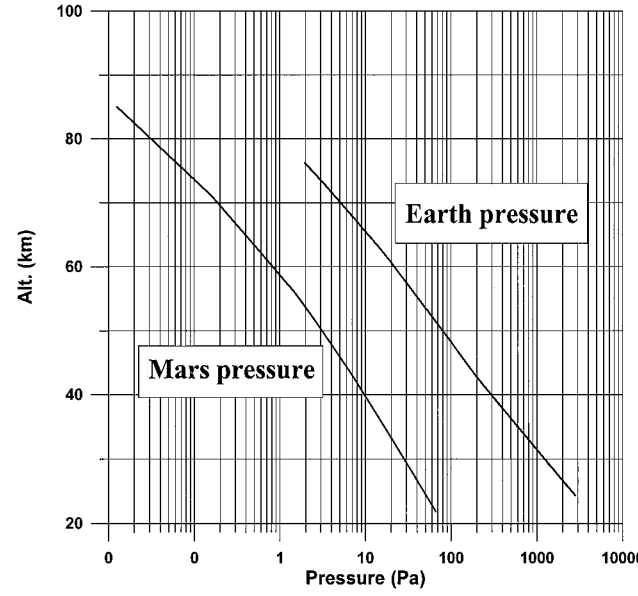

Fig. 3 Pressures in Mars and Earth atmospheres.

body flowfield is dominated by the presence of the strong bow shock wave and the consequent heating.[1]

At high-altitude hypersonic flight conditions, the vibrational energies excitation and chemical reactions occur slowly enough that a significant portion of the flowfield is in a state of thermochemical nonequilibrium. Another important effect is related to the catalytic activity of the wall; indeed, the wall may act like a catalyst promoting the recombination of the atomic species. It is well known that the effect of catalycity during Earth reentry[2] can result in an increase in the heat flux up to 100%. The authors believe that catalytic effects may be even larger in Martian atmosphere because 1) pressure in Martian atmosphere is lower than that of Earth (nonequilibrium effects are consequently enhanced) and 2) the characteristic dissociation temperature of CO_2 ($T_{d\,CO_2} = 64{,}000$ K) is lower than that of N_2 (the main component of air, $T_{d\,N_2} = 114{,}000$ K), and the concentration of dissociated species in the vicinity of the wall is larger in a CO_2 environment when compared to air.

There are many published results on aerothermodynamic heating for a vehicle entering the Martian atmosphere.[3–10] Some of the literature addresses the problem of the enhanced heating rates due to surface catalycity, which seems to have much importance on the aerothermal environment of the vehicle.[7–10]

These aspects have been investigated, numerically and experimentally, in the present work. In the first part, the model used for the reacting gas mixture is presented, and the numerical code used to solve the governing equations is described. In the second part, typical trajectories in Mars atmosphere are calculated, and heat fluxes and heat loads are derived, with considerations of thermal and chemical nonequilibrium effects, and catalytic effects. Finally, the Small Planetary Entry Simulator (SPES) plasma wind tunnel is described, and preliminary experimental results on test models with different catalytic properties in a prevalent CO_2 environment, and the related numerical correlations, are discussed.

Thermodynamic Model

An aerothermochemical model for the Mars atmosphere was prepared, considering a gas mixture composition of eight chemical species: CO_2, CO, O, C, O_2, N_2, N, and NO. The atmosphere was modeled as a mixture of perfect gases for which Dalton's law is applicable:

$$p = \sum_i p_i \tag{1}$$

where the summation is extended to all of the species considered. As a consequence, the following relation holds:

$$\rho = p \Big/ R_0 T \sum_i \frac{m_i}{M_i} \tag{2}$$

The internal energy of the mixture is defined as

$$e = \sum_i (m_i e_i) \tag{3}$$

where e_i, the internal energy of the single component gas, is the sum of the energies representing the different degrees of the freedom of the molecules:

$$e_i = e_{\mathrm{tr},i} + e_{\mathrm{rot},i} + e_{v,i} + e_{e,i} + e_{0,i} \tag{4}$$

In our model we assume that the translational, rotational, and electronic modes are in equilibrium at the temperature T, whereas polyatomic molecules may vibrate at a temperature T_v different from T. From quantum mechanics through the partition function[11,12] the expression for each of the energy terms becomes

$$e_{\mathrm{tr},i} = \frac{3}{2} R_i T \tag{5}$$

$$e_{\mathrm{rot},i} = R_i T \tag{6}$$

$$e_{v,i} = \frac{R T^c_{v,i}}{\exp\left(T^c_{v,i}/T_v\right) - 1} \tag{7}$$

$$e_{e,i} = \frac{R_i}{Q_{e,i}} \left\{ g_{1,i}\Theta_i(1) \exp\left[-\frac{\Theta_i(1)}{T}\right] - g_{2,i}\Theta_i(2) \exp\left[-\frac{\Theta_i(2)}{T}\right] \right\} \tag{8}$$

From these expressions the specific enthalpy for each species may be calculated as

$$h_i = e_i + R_i T \tag{9}$$

Field Equations

The fluid has been modeled as a reacting gas in thermal and chemical nonequilibrium, and so the equations considered are the balance equations for mass, single chemical species, momentum, vibrational energy, and total energy (less the vibration). They are written as follows.

Continuity:

$$\frac{\partial \rho}{\partial t} + \nabla \cdot (\rho \boldsymbol{V}) = 0 \tag{10}$$

Species:

$$\frac{\partial (\rho m_i)}{\partial t} + \nabla \cdot (\rho \boldsymbol{V} m_i) + \nabla \cdot \boldsymbol{J}_i = \dot{\omega}_i \tag{11}$$

Momentum:

$$\frac{\partial (\rho \boldsymbol{V})}{\partial t} + \nabla \cdot (\rho \boldsymbol{V}\boldsymbol{V}) + \nabla p = 2\nabla \cdot \left[\mu (\nabla \boldsymbol{V})_0^s\right] \tag{12}$$

where

$$(\nabla \boldsymbol{V})_0^s = \tfrac{1}{2}[(\nabla \boldsymbol{V}) + (\nabla \boldsymbol{V})^T] - \tfrac{1}{3}(\nabla \cdot \boldsymbol{V})\underline{\underline{U}} \tag{13}$$

Energy:

$$\frac{\partial (\rho E)}{\partial t} + \nabla \cdot [(\rho E + p)\boldsymbol{V}] = \nabla \cdot \left[\lambda \nabla T + 2\mu (\nabla \boldsymbol{V})_0^s \cdot \boldsymbol{V} + \sum_i h_i \boldsymbol{J}_i \right] - \sum_i h_i \dot{\omega}_i - \sum_j \dot{e}_{v_j} \tag{14}$$

Vibrational energy:

$$\frac{\partial \left(\rho e_{v_j}\right)}{\partial t} + \nabla \cdot \left(\rho \boldsymbol{V} e_{v_j}\right) = \dot{e}_{v_j} \tag{15}$$

Transport Properties

Computation of the diffusive fluxes requires knowledge of the transport coefficients. For pure species, the following expressions are derived from the kinetic theory of gases.[13]

Viscosity:

$$\mu_i = \frac{2.6693 \cdot 10^{-6} \sqrt{M_i T}}{\sigma_i^2 \Omega_{\mu i}} \tag{16}$$

Thermal conductivity:

$$\lambda_i = \tfrac{15}{4}(\mu_i R_0 / M_i)\left[\tfrac{4}{15}(c_{pi} M_i / R_0) + \tfrac{1}{3}\right] \tag{17}$$

Mass diffusivity:

$$D_{ij} = \frac{0.0188 \cdot T^{\frac{3}{2}} \sqrt{(M_i + M_j)/M_i M_j}}{p \sigma_{ij}^2 \Omega_{Dij}} \tag{18}$$

The transport model was chosen as a tradeoff between accuracy and computational efficiency among well-established transport models for Martian atmosphere.[14,15]

When one considers the global transport properties of the mixture, semi-empirical rules may be applied, such as Wilke's rule for viscosity and thermal conductivity:

$$\mu, \lambda = \frac{\sum_i \chi_i (\mu_i, \lambda_i)}{\sum_j \chi_j \left(\frac{1}{\sqrt{8}} (1 + M_i/M_j)^{-\frac{1}{2}} \left\{ 1 + [(\mu_i, \lambda_i)/(\mu_j, \lambda_j)]^{\frac{1}{2}} (M_j/M_i)^{\frac{1}{4}} \right\}^2 \right)} \tag{19}$$

For the diffusion coefficient of the species i in the mixture, the following relation may be applied:

$$D_i = (1 - \chi_i) \Big/ \sum_j \frac{\chi_j}{D_{i,j}} \tag{20}$$

Chemical and Vibrational Nonequilibrium Models

The chemical production rate of species i in reaction k is

$$\dot{\omega}_{ik} = \Gamma (\nu''_{ik} - \nu'_{ik}) \cdot \left[K_{fk} \prod_j C_j^{\nu'_{jk}} - K_{bk} \prod_j C_j^{\nu''_{jk}} \right] \tag{21}$$

where K_{fk} and K_{bk} are the forward and backward rate constants for the kth reaction, modeled according to the Arrhenius law:

$$K_k = A_K T^{\beta_K} \exp[-(E_k/R_0 T)] \tag{22}$$

The source term for species i appearing in the species balance equations is then written as

$$\dot{\omega}_i = M_i \sum_k \dot{\omega}_{ik} \tag{23}$$

The primary source for reaction-rate data constants is by Park[16]; the reactions considered are reported in Table 1.

For the vibrational thermal relaxation, the Landau–Teller model was used,

$$\dot{e}_{vs} = \rho \frac{e^*_{vs} - e_{vs}}{\tau_s} \tag{24}$$

where e^*_{vs} is the vibrational energy evaluated at the temperature T.

The vibrational characteristic time is computed by the Millikan and White semi-empirical formula:

$$\tau_s = \frac{\sum_r \chi_r}{\sum_r \chi_r / \tau_{sr}} \tag{25}$$

where

$$\tau_{sr} = (1/p) \exp\left[0.00116 \mu_{sr}^{\frac{1}{2}} \theta_s^{\frac{4}{3}} \left(T^{-\frac{1}{3}} - 0.015 \mu_{sr}^{\frac{1}{4}} \right) - 18.42 \right] \tag{26}$$

Table 1 Forward rate constants

Reaction	Third body	A_k	$T_{d,k}$, K	N
$CO_2 + M \rightarrow CO + O + M$	M^a	6.9×10^{18}	63,275	−1.5
$CO_2 + M \rightarrow CO + O + M$	M^b	1.4×10^{19}	63,275	−1.5
$CO + M \rightarrow C + O + M$	M^a	2.3×10^{17}	129,000	−1.0
$CO + M \rightarrow C + O + M$	M^b	3.4×10^{17}	129,000	−1.0
$N_2 + M \rightarrow N + N + M$	M^a	7.0×10^{18}	113,200	−1.6
$N_2 + M \rightarrow N + N + M$	M^b	3.0×10^{19}	113,200	−1.6
$O_2 + M \rightarrow O + O + M$	M^a	2.0×10^{18}	59,750	−1.5
$O_2 + M \rightarrow O + O + M$	M^b	1.0×10^{19}	59,750	−1.5
$NO + M \rightarrow N + O + M$	M^a	5.0×10^{12}	75,500	0.0
$NO + M \rightarrow N + O + M$	M^b	1.1×10^{14}	75,500	0.0
$NO + O \rightarrow N + O_2$	——	8.4×10^{9}	19,450	0.0
$N_2 + O \rightarrow NO + N$	——	6.4×10^{14}	38,370	−1.0
$CO + O \rightarrow O_2 + C$	——	3.9×10^{10}	69,200	−0.18
$CO_2 + O \rightarrow O_2 + CO$	——	2.1×10^{10}	27,800	0.0

[a] $M = CO_2$, CO, N_2, O_2, NO. [b] $M =$ C, N, O.

Table 2 Comparison between computed and free-flight extrapolated surface temperatures at the stagnation point

	T_w, K	
t, s (z, km)	Computed	Pathfinder
50 (57)	1360	1200
55 (51)	1650	1500
66 (41)	2080	2100
71 (36)	1800	1850
80 (30)	1650	1600

and

$$\mu_{sr} = M_s M_r / (M_s + M_r) \tag{27}$$

is the reduced molecular weight.

Boundary Conditions

Species boundary conditions on the wall have been assigned to model the two extreme behaviors of a solid surface. First, in the case of a fully catalytic wall, the species concentrations at the wall have been set equal to the freestream composition (95% CO_2 and 5% N_2, for Martian atmospheric entry). Second, for a noncatalytic wall, the diffusive flux of atoms at the wall is set to zero.

Radiative equilibrium has been assumed for the wall surfaces to evaluate the wall temperature. The thermal protection system (TPS) material is a low-density ablator, called superlight ablator (SLA), 561 V (Refs. 17 and 18). This material consists of a fiberglass phenolic honeycomb with about 1-cm cells that are packed with a charring ablative compound containing elastomeric silicone and various fillers. The surface emissivity is 0.9 (Ref. 18), and this value is used throughout the computations. Table 2 shows the computed average surface temperatures (for a fully catalytic wall) at the capsule stagnation point. The temperatures are compared to the surface temperature data reported in Ref. 19 that have been predicted through the nine type-K thermocouples inside the TPS of the Pathfinder using well-validated thermal response codes.[19]

Numerical Technique

The preceding equations with the appropriate boundary conditions have been solved with the numerical code Fluent,[20] which solves by a finite volume method a system of partial differential equations:

$$\frac{\partial \tilde{\boldsymbol{U}}}{\partial t} + \frac{1}{V}\sum_i (\bar{\boldsymbol{F}} - \bar{\boldsymbol{G}})_i \cdot \boldsymbol{A}_i = \tilde{\boldsymbol{H}} \tag{28}$$

Nondissipative fluxes are computed according to the flux difference splitting technique proposed by Roe.[21] Dissipative fluxes are computed by the Gauss theorem. Accuracy is second order in space. Time integration is performed by an explicit multistage Runge–Kutta scheme. Multigrid techniques are used to accelerate convergence. Generally, accurate computations of the gradients appearing in the field equations require structured grids, which have been used for all computations in the present work. The computation of the heat transfer or skin friction requires detailed resolution of the flow very near the surface. An iterative approach was followed to determine the near-body grid resolution, which provides grid-solution independence. In the present computations, the value of the grid spacing near the wall was found to be 10^{-6} m. Grid refinement in strong gradient regions was made when necessary through a solution adaptive approach.

Validation of the Model

The model has been validated through comparison with published numerical results of heat fluxes on a well-known Mars entry capsule, the Mars Pathfinder (Fig. 4), for which a number of experimental and numerical results are available.

The Mars Pathfinder successfully completed entry, descent, and landing on the Martian surface on 4 July 1997. The primary objective of the probe mission was to demonstrate a low-cost, reliable system for landing on the surface of Mars.[22–24] The geometry of the probe is shown in Fig. 5. The forebody is a sphere–cone shape with a nose radius of 0.66 m and a half-angle cone of 70 deg; the afterbody is a truncated cone with a half-angle of 46 deg. The mesh used for the numerical computations is shown in Fig. 6. Conditions used for the numerical simulations are representative of the point of Pathfinder trajectory corresponding to the peak heat flux and are summarized in Table 3.

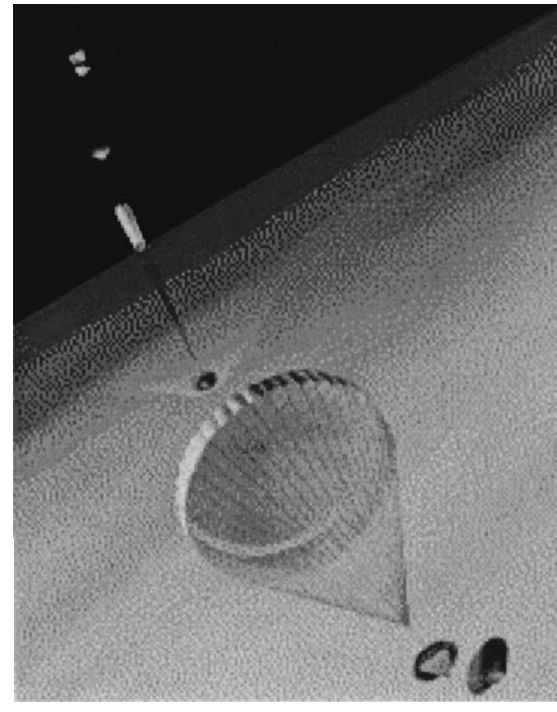

Fig. 4 Mars Pathfinder entry in the Martian atmosphere.

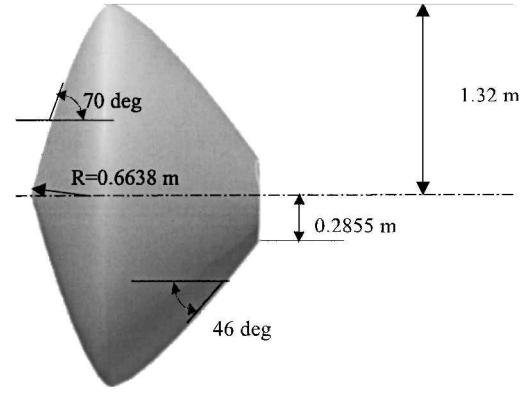

Fig. 5 Mars Pathfinder geometry.

Table 3 Pathfinder peak heat flux freestream conditions

Parameter	Value
Time	66 s
Altitude	41 km
Mach number	32
Temperature	170 K
Density	2.8×10^{-4} kg/m^3

Table 4 F4 nozzle flow conditions

Parameter	Value
Stagnation pressure, bar	373
Total enthalpy, MJ/kg	11
Wall temperature, K	300
Test chamber pressure, Pa	68
Test chamber temperature, K	300

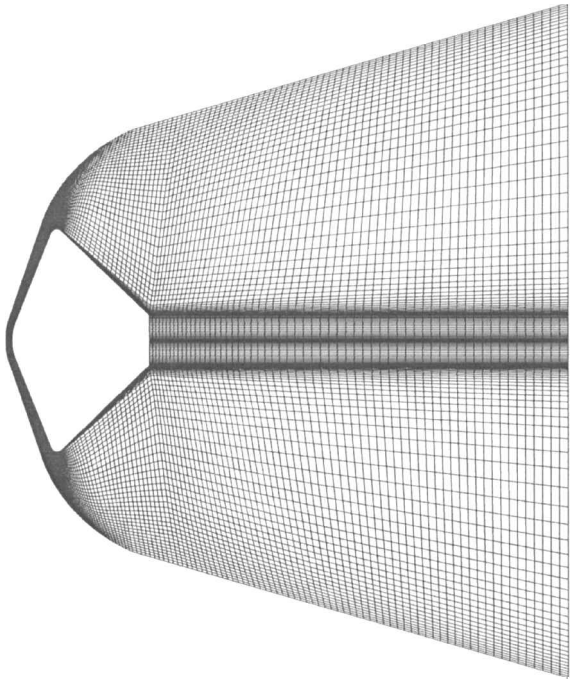

Fig. 6 Mesh for the numerical computations.

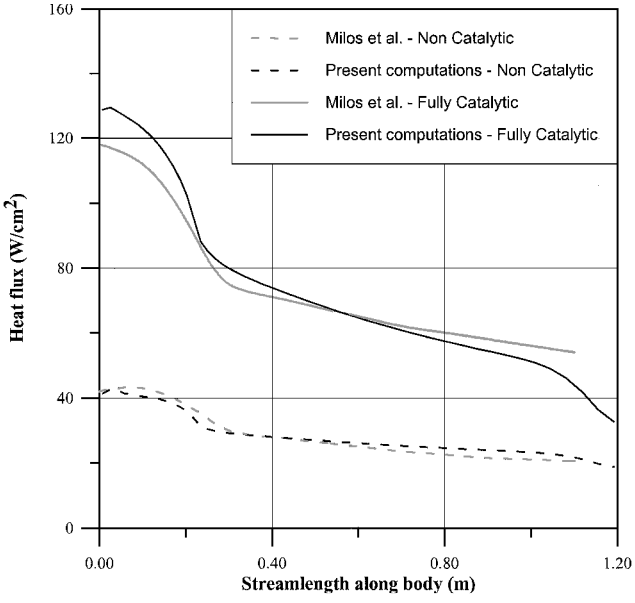

Fig. 7 Comparison of numerical results on heat fluxes along the Mars Pathfinder forebody.

Table 5 Starting point for trajectory calculations

Parameter	Value
Altitude	130 km
Velocity	7.5 km/s
Entry angle	From −11 to −20 deg

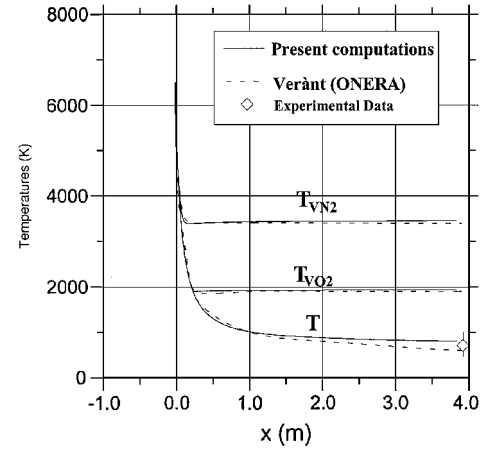

Fig. 8 Translational and vibrational temperature comparison along the axis of the F4 nozzle.

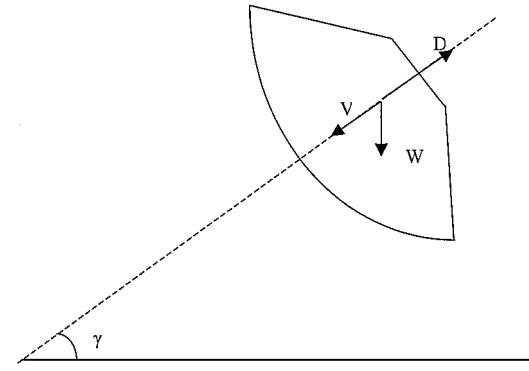

Fig. 9 Forces acting on the ballistic entry vehicle.

Figure 7 shows the comparison of heat fluxes along the Pathfinder forebody between the present computation and numerical results from Milos et al.[19] The heat fluxes are evaluated at the two extreme conditions of noncatalytic and fully catalytic walls.

The nonequilibrium vibration model has been validated by comparisons with benchmark results for a hypersonic wind-tunnel nozzle flow presented in Ref. 25. The axisymmetric airflow in thermal and chemical nonequilibriumin the F4 wind-tunnel nozzle has been studied, and the conditions of the test case are reported in Table 4. Temperature distributions along the nozzle axis are shown in Fig. 8.

Trajectory Calculations

Entry trajectories in the Mars atmosphere have been calculated for a ballistic vehicle (the Mars Pathfinder; $B = 63.5$ kg/m^2). The ordinary differential equations of motion for a point mass subjected to gravity and aerodynamic drag (Fig. 9 provides reference to symbols used):

$$W \cos\gamma = m\dot{\gamma}V \tag{29}$$

$$-D + W \sin\gamma = m\dot{V} \tag{30}$$

have been numerically integrated by the Euler method, starting from the conditions reported in Table 5.

For the freestream density, an exponential function of altitude was obtained by interpolating the reconstructed martian atmospheric data[24]:

$$\rho = \rho_0 \exp(-\beta z) \tag{31}$$

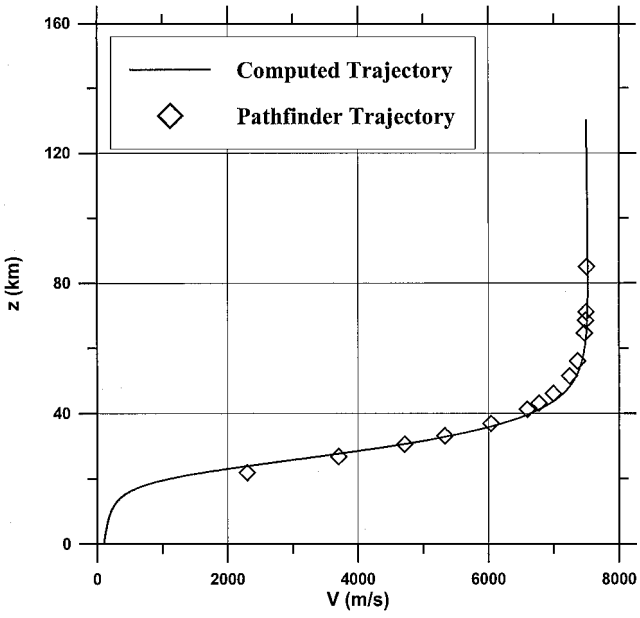

Fig. 10 Mars Pathfinder computed and reconstructed trajectories.

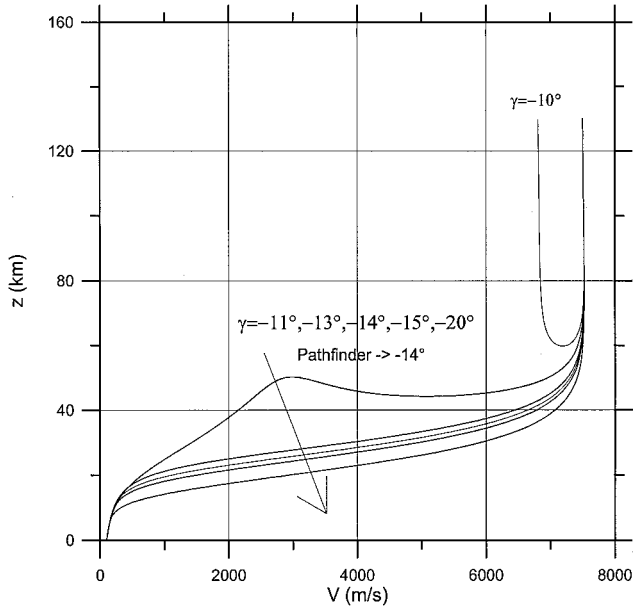

Fig. 11 Entry trajectories for different entry angles.

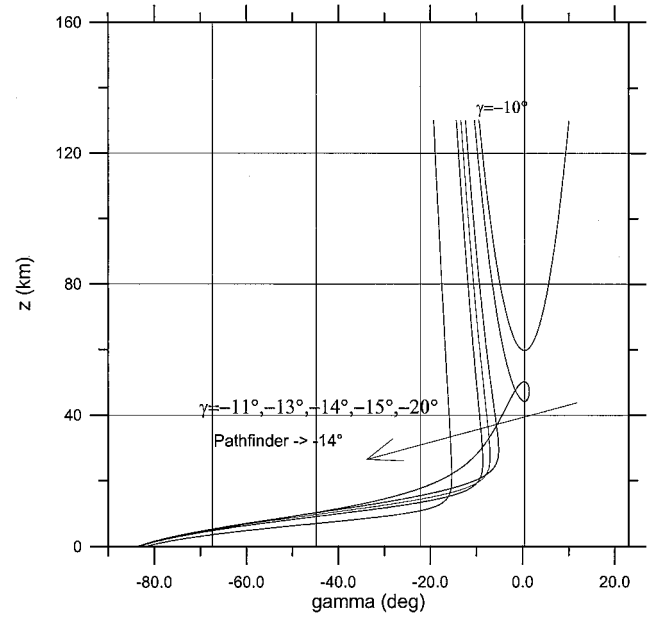

Fig. 12 Flight-path angles for each trajectory.

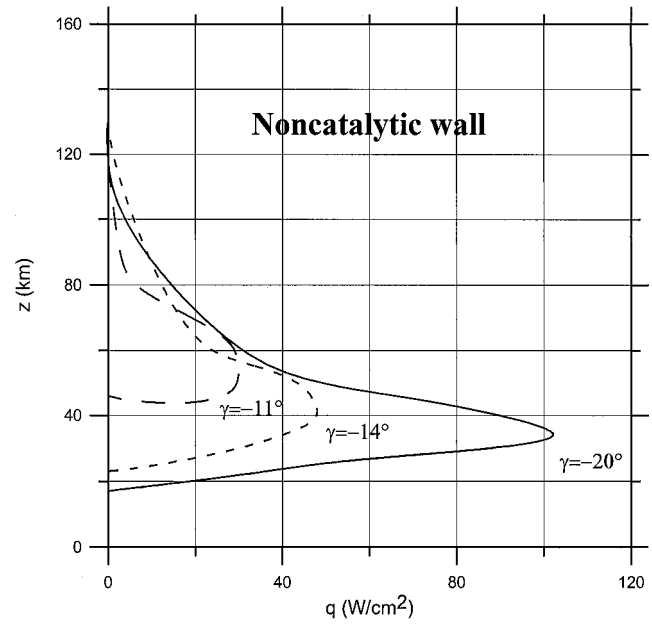

Fig. 13 Noncatalytic stagnation-point heat fluxes for different entry trajectories.

The trajectory calculation code has been validated by comparing the results corresponding to an entry angle of −14 deg (the Pathfinder entry angle) with the Pathfinder trajectory[24] (Fig. 10), which has been reconstructed from onboard measurements (two sets of three orthogonally positioned accelerometers and a radar altimeter[24]).

A number of entry trajectories have been calculated corresponding to several entry flight-path angles, starting from the minimum angle needed to enter the Mars atmosphere (−11 deg) to an entry angle of −20 deg corresponding to the maximum deceleration level. Shown in Fig. 11 is the velocity–altitude plot for the computed trajectories. The trajectory corresponding to an entry angle of −10 deg is also plotted, to show that the vehicle considered would skip the entry at that initial entry angle. Figure 12 shows the flight-path angles for each of the considered trajectories.

Numerical Computations

For each of the computed trajectories, Navier–Stokes flowfield computations were performed at discrete altitudes. Stagnation-point heat fluxes for noncatalytic and fully catalytic surfaces have been computed for each of these trajectories (Figs. 13 and 14). Figures 13 and 14 show that, for increasing entry angle magnitude, the peak heat fluxes increase. Figures 15–17 highlight the substantial decrease in heat flux that a noncatalytic wall would experience with respect to a fully catalytic surface. Figure 18 shows the peak heat flux for each trajectory as a function of the entry angle. It can be seen that, in both cases of fully catalytic and noncatalytic wall, the heat fluxes increase with the entry angle magnitude.

The percentage of the heat flux due to the wall catalytic properties can be evaluated by the nondimensional ratio

$$\dot{q}_{FC}/\dot{q}_{NC}$$

At the typical entry angle of the Pathfinder mission (−14 deg) the value of this ratio is about 3, so that the catalytic behavior of the surface may change the heat flux up to 300%. Figure 19 shows that to minimize the heat fluxes a trajectory close to the minimum entry angle (−11 deg) should be chosen.

The overall thermal load per unit area, Q, can be defined as

$$Q = \int_{t_1}^{t_2} \dot{q}\, dt \tag{32}$$

Figure 19 shows that Q, contrary to the heat flux, is a decreasing function of the entry angle. This behavior can be explained by

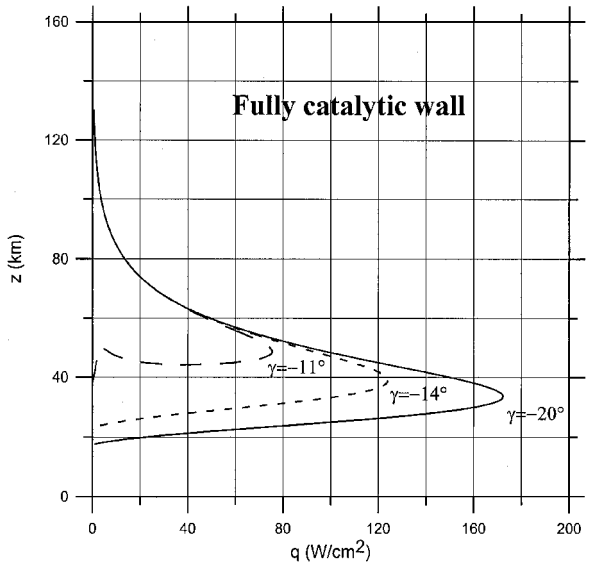

Fig. 14 Fully catalytic stagnation-point heat fluxes for different entry trajectories.

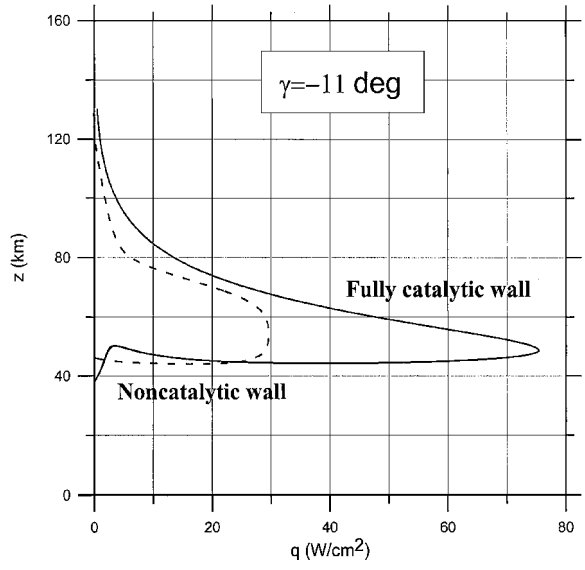

Fig. 15 Comparison of noncatalytic and fully catalytic stagnation-point heat fluxes ($\gamma = -11$ deg).

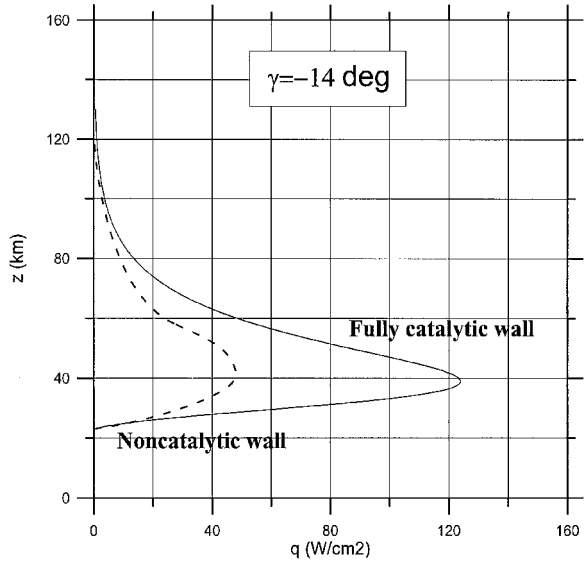

Fig. 16 Comparison of noncatalytic and fully catalytic stagnation-point heat fluxes ($\gamma = -14$ deg).

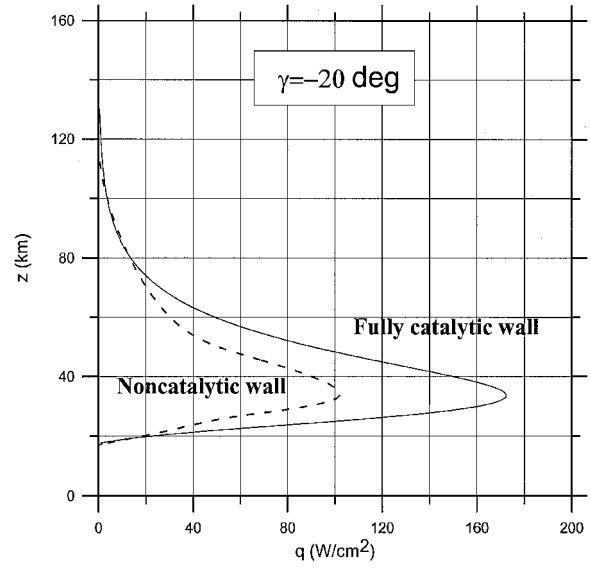

Fig. 17 Comparison of noncatalytic and fully catalytic stagnation-point heat fluxes ($\gamma = -20$ deg).

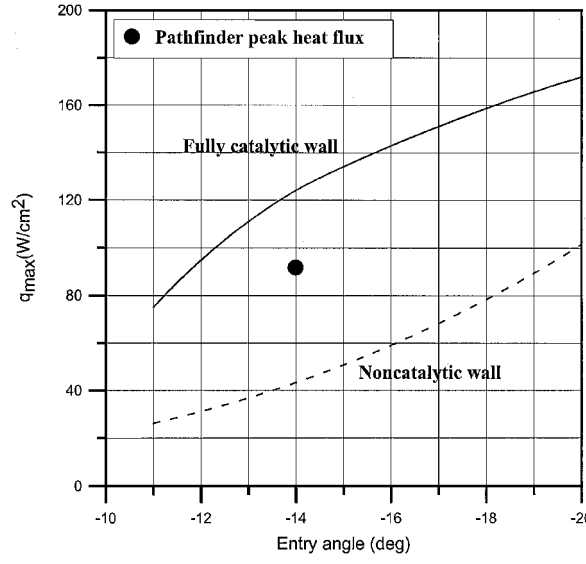

Fig. 18 Peak heat fluxes vs entry angle.

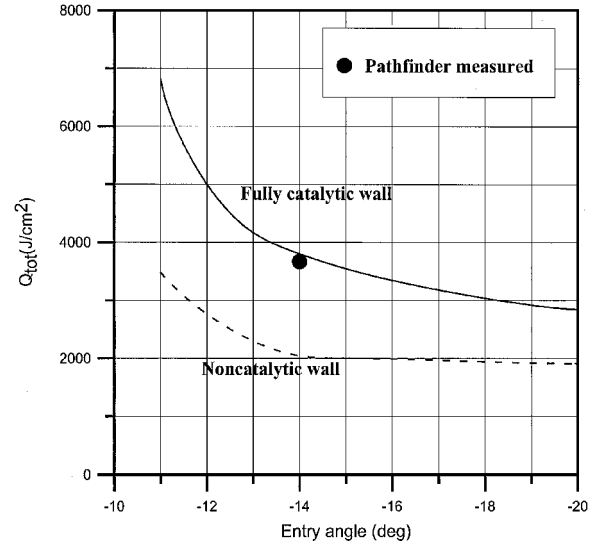

Fig. 19 Thermal load as a function of entry angle.

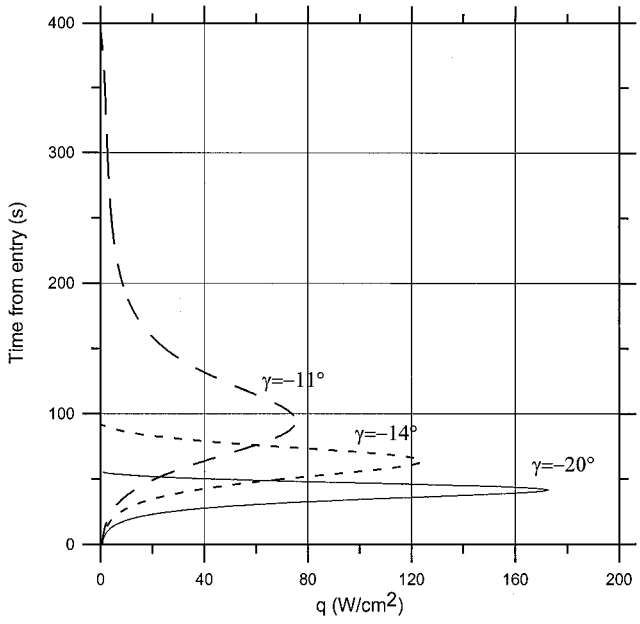

Fig. 20 Heat flux vs time for fully catalytic wall.

Fig. 20. At higher entry angles, the peak heat fluxes increase, but the trajectory total time is reduced so that the integrated thermal load decreases.

Therefore, if one is interested in minimizing the heat fluxes, a trajectory characterized by a low entry angle should be chosen, whereas if one wants to minimize the thermal load, trajectories at larger entry angles should be considered.

Experimental Tests

Experimental tests have been performed in the SPES facility at the Department of Space Science and Engineering.[26] The facility is a continuous, open-circuit, blowdown arc facility. It consists of a 40-kW plasma torch where the primary gas is supplied and heated, a swirl mixer where the secondary gas is supplied to obtain the desired atmospheric composition, a convergent–divergent nozzle where the flow expands to a nominal Mach number of 3, and a test chamber instrumented with total pressure probes and heat flux probes. Two types of heat flux probes were used:

1) Gardon gauges consist basically of a thin metallic foil suspended in a heat sink (copper) in the form of a hollow cylinder (Fig. 21). The metallic foil, as the first thermoelectric material (constantan), creates, together with the second thermoelectric material (copper), one junction of the thermocouple. A wire of the second thermoelectric material is attached to the rear surface center of the foil to form a differential thermocouple. It measures the temperature difference between the center and the edge of the foil, which can be correlated to the heat flux on the constantan foil.

2) Slug calorimeters of different materials (tungsten and silver), measure the slope of the back surface temperature history of the calorimetric model, generally a copper cylinder (Fig. 22). A thermocouple is attached to the backface of the sensor. The calorimetric mass is integrated in a thermal insulator to avoid radial heat losses. Figure 23 is a photograph of the jet in the test chamber.

Two experimental runs were performed using mixtures of different composition. The test conditions are summarized in Table 6. The primary gas is nitrogen, the secondary jet is air or CO_2. For the latter case a Martianlike composition is simulated. The goal is the measurement of the stagnation-point heat fluxes on test models of different catalytic properties to highlight different catalytic effects in both mixtures.

At the same time, numerical computations were performed to correlate the experimental results. The meshes and boundary conditions used for the computations are shown in Figs. 24 and 25. A mixture with an average specific enthalpy of 14 MJ/kg is formed by mixing 0.3 g/s of the primary gas (nitrogen), with specific total

Table 6 Experimental test conditions

Test gas	Mass flow rate, g/s		Average specific total enthalpy, MJ/kg
	Primary	Secondary	
$N_2 + Air$	N_2 (0.3)	Air (0.9)	14
$N_2 + CO_2$	N_2 (0.3)	CO_2 (0.9)	14

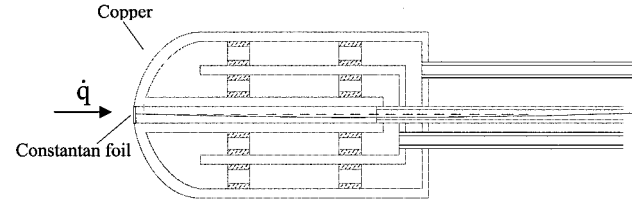

Fig. 21 Gardon gauge.

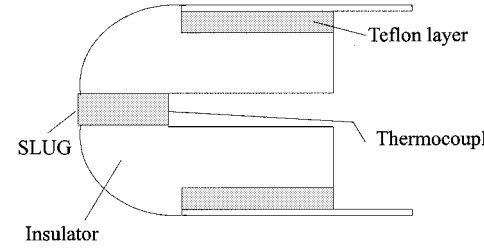

Fig. 22 Slug calorimeter.

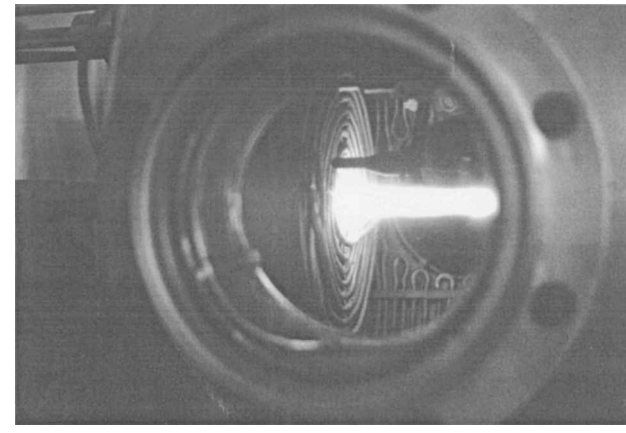

Fig. 23 Plasma jet in the test chamber.

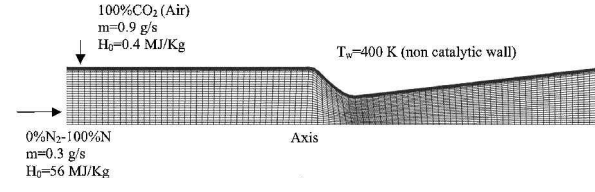

Fig. 24 Nozzle geometry and mesh and boundary conditions.

enthalpy of 56 MJ/kg, and 0.9 g/s of the cold secondary jet, with specific total enthalpy of 0.3 MJ/kg.

The experimental results show that the measured stagnation-point heat fluxes in mixtures with CO_2 are always lower than the corresponding values measured in air mixtures. The numerical computations are in agreement with the experimental results and show that this behavior can be explained by the larger dissociation occurring in CO_2 mixtures. Indeed, looking at the computed temperature distributions as shown in Fig. 26, one can observe that the temperature at the nozzle exit and in the shock layer, for the CO_2 mixture, is lower than in the air mixture.

As a consequence, if the surface of the model is noncatalytic to atom recombination, a lower heat flux on the model surface in a CO_2 environment is expected. The materials of the test models (silver,

Table 7 Experimental results and numerical correlations in SPES facility

Parameter	Experimental results	Numerical results
	Mixture $N_2 + CO_2$	
Mixer pressure, Pa	18,862 ± 100	20,128
Exit nozzle pressure, Pa	920 ± 100	960
Stagnation-point pressure, Pa	6,705 ± 100	6,825
Heat flux, kW/m^2	1,180 ± 200 (tungsten model)	1,400 (noncatalytic wall)
Heat flux, kW/m^2	2,200 ± 330 (silver model)	4,300 (fully catalytic wall)
	Mixture $N_2 + air$	
Mixer pressure, Pa	19,968 ± 100	20,395
Exit nozzle pressure, Pa	880 ± 100	910
Stagnation-point pressure, Pa	7,371 ± 100	7,531
Heat flux, kW/m^2	2,235 ± 335 (tungsten model)	2,500 (noncatalytic wall)
Heat flux, kW/m^2	3,050 ± 450 (silver model)	4,500 (fully catalytic wall)

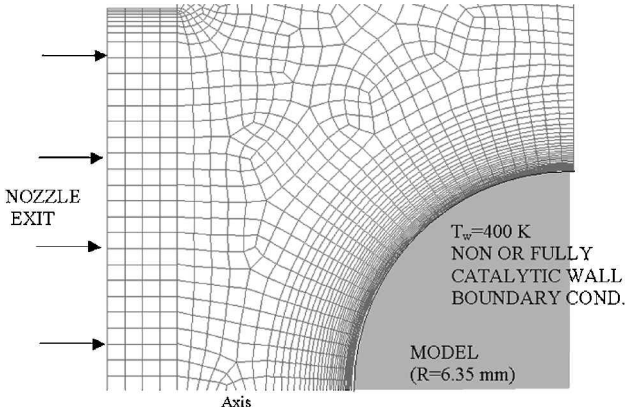

Fig. 25 Test chamber mesh and boundary conditions.

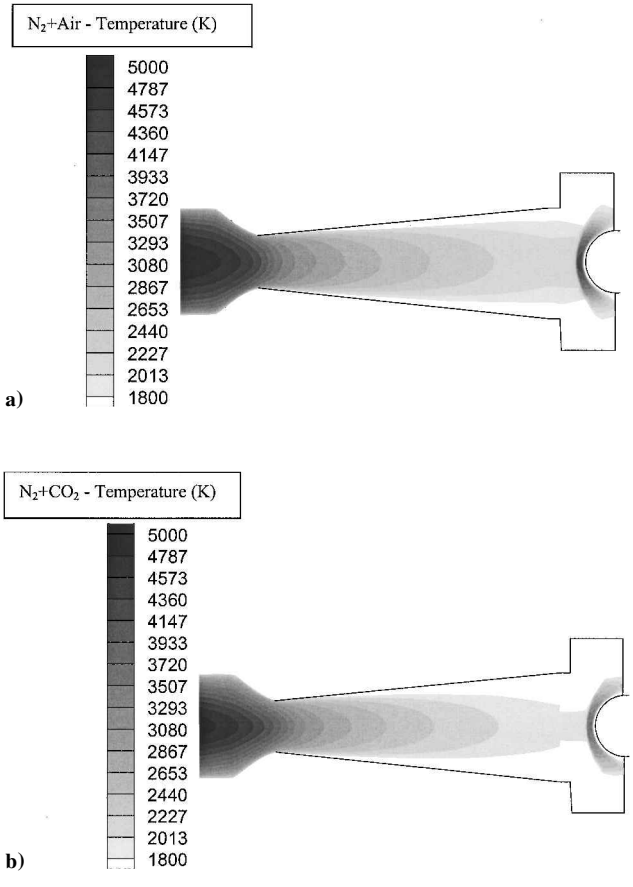

Fig. 26 Temperature distributions in SPES nozzle and test chamber for a) air mixture and b) CO_2 mixture.

constantan, and tungsten) have different catalytic behavior, silver being the most catalytic and tungsten the least catalytic material (for air). As expected, stagnation-point heat fluxes were lower in the simulated Martian atmosphere. Table 7 is a summary of the experimental results and the numerical correlations.

The percentage of the heat flux due to catalycity appears to be greater in the simulated Martian atmosphere than in air.

CO_2 mixture :

$$\dot{q}_{FC}/\dot{q}_{NC} = 3.1$$

Air:

$$\dot{q}_{FC}/\dot{q}_{NC} = 1.8$$

These results confirm that a larger influence of the surface catalycity is to be expected in a Marslike atmosphere.

Conclusions

A mathematical and physical model has been developed to study the entry of a space vehicle in the Mars atmosphere. The influence of the surface catalycity effects on heat fluxes and heat loads has been assessed for typical trajectories for a reference entry ballistic vehicle. Results show that the catalycity can provide important guidelines for the aerothermodynamic design of a Mars entry vehicle. In particular, if one is concerned with the minimization of the heat flux, entry trajectories characterized by low entry angles should be chosen; if one is interested in minimizing the heat load, higher entry angle trajectories should be considered. Experimental results obtained in a plasma wind tunnel and the related numerical correlations confirm the greater importance of the surface catalycity effects in a Martianlike atmosphere with respect to the Earth atmosphere.

References

[1]"Capsule Aerothermodynamics," Rept. 808, AGARD, May 1997.

[2]Scott, C. D., "A Review of Nonequilibrium Effects and Surface Catalysis on Shuttle Heating," NASA CP-2283, Pt. 2, March 1983.

[3]Hollis, B. R., "Experimental and Computational Aerothermodynamics of a Mars Entry Vehicle," NASA CR-201633, Dec. 1996.

[4]Mitcheltree, R. A., "Aerothermodynamic Methods for a Mars Environmental Survey Mars Entry," *Journal of Spacecraft and Rockets*, Vol. 31, No. 3, 1994, pp. 516–523.

[5]Mitcheltree, R. A., DiFulvio, M., Horvath, T. J., and Braun, R. D., "Aerothermal Heating Predictions for Mars Microprobe," *Journal of Spacecraft and Rockets*, Vol. 36, No. 3, 1999, pp. 405–411.

[6]Chen, Y. K., Henline, W. D., and Tauber, M. E., "Mars Pathfinder Trajectory Based Heating and Ablation Calculations," *Journal of Spacecraft and Rockets*, Vol. 32, No. 2, 1995, pp. 225–230.

[7]Chen, Y. K., Henline, W. D., Stewart, D. A., and Candler, G. V., "Navier–Stokes Solutions with Surface Catalysis for Martian Atmospheric Entry," *Journal of Spacecraft and Rockets*, Vol. 30, No. 1, 1993, pp. 32–42.

[8]Gupta, R. N., Lee, K. P., and Scott, C. D., "Aerothermal Study of Mars Pathfinder Aeroshell," NASA TM-111461, Jan. 1995.

[9]Kay, R. D., and Netterfield, M. P., "Thermochemical Non-Equilibrium Computations for a Mars Entry Vehicle," AIAA Paper 93-2841, 1993.

[10]Chen, Y.-K., "Effect of Non-Equilibrium Flow Chemistry on the Heating Distribution over the MESUR Forebody During a Martian Entry," NASA CR-177601, Sept. 1992.

[11]Anderson, J. D., Jr., *Hypersonic High Temperature Gas Dynamics*, McGraw–Hill, New York, 1989, pp. 413–481.

[12]Park, C., *Nonequilibrium Hypersonic Aerothermodynamics*, Wiley, New York, 1990, pp. 43–88.

[13]Hirschfelder, J. O., Curtiss, C. F., and Bird, R. B., *Molecular Theory of Gases and Liquids*, Wiley, New York, 1954, pp. 75–106.

[14]Candler, G., "Computation of Thermo-Chemical Nonequilibrium Martian Atmospheric Entry Flows," AIAA Paper 90-1965, 1990.

[15]Riabov, V. V., "Approximate Calculation of Transport Coefficients of Earth and Mars Atmospheric Dissociating Gases," *Journal of Thermophysics and Heat Transfer*, Vol. 10, No. 2, 1996, pp. 209–216.

[16]Park, C., "Review of Chemical-Kinetics Problems of Future NASA Missions, Part 2: Mars Entries," *Journal of Thermophysics and Heat Transfer*, Vol. 8, No. 1, 1994, pp. 9–23.

[17]Congdon, W. M., "SLA-561V Thermal Ablation Model: Sensitivity Study of Model Parameters," Applied Research Associates, Inc., Albuquerque, NM, Oct. 1994.

[18]Congdon, W. M., Edquist, C. T., and Henline, W. D., "Thermal Protection Studies for the 1996 Pathfinder Mission to Mars," AIAA Paper 94-0249, 1994.

[19]Milos, F. S., Chen, Y.-K., Congdon, W. M., and Thornton, J. M., "Mars Pathfinder Entry Temperature Data, Aerothermal Heating, and Heatshield Material Response," *Journal of Spacecraft and Rockets*, Vol. 36, No. 3, 1999, pp. 380–391.

[20]"Fluent 5 User's Guide," Fluent Inc., Lebanon, NH, 1998.

[21]Roe, P. L., "Characteristic Based Schemes for the Euler Equations," *Annual Review of Fluid Mechanics*, Vol. 18, 1986, pp. 337–365.

[22]Vaughan, R. M., Kallemeyn, P. H., Jr., Spencer, D. A., and Braun, R. D., "Navigation Flight Operations for Mars Pathfinder," *Journal of Spacecraft and Rockets*, Vol. 36, No. 3, 1999, pp. 340–347.

[23]Braun, R. D., Spencer, D. A., Kallemeyn, P. H., and Vaughan, R. M., "Mars Pathfinder Atmospheric Entry Navigation Operations," *Journal of Spacecraft and Rockets*, Vol. 36, No. 3, 1999, pp. 348–356.

[24]Spencer, D. A., Blanchard, R. C., Braun, R. D., Kallemeyn, P. H., and Thurman, S. W., "Mars Pathfinder Entry, Descent, and Landing Reconstruction," *Journal of Spacecraft and Rockets*, Vol. 36, No. 3, 1999, pp. 357–366.

[25]Sagnier, P., "Synthesis of the Contributions to the Test Case T10-97 Wind Tunnel Nozzle," *Proceedings of the First Europe–U.S. High Speed Database Workshop*, Pt. 2, Naples, Italy, 1997, pp. 466–474.

[26]Paterna, D., "Planetary Atmospheric Entry Simulation by a Small Pilot Facility," Dept. of Space Science and Engineering, "Luigi G. Napolitano," DISIS Internal Rept. 2000-01, Univ. of Naples "Federico II," Naples, Italy, July 2000.

M. Torres
Associate Editor